

ARTICLE OPEN

Artificial creation and separation of a single vortex–antivortex pair in a ferroelectric flatland

Jeongyong Kim^{1,2}, Mujin You^{1,2}, Kwang-Eun Kim^{1,2}, Kanghyun Chu^{1,2} and Chan-Ho Yang^{1,2,3}

Topological defects have received much attention due to their stability against perturbations and potential applications in nonvolatile high-density memory. Topologically non-trivial textures can be compelled by constraints on boundary condition, geometrical structure, and curved space. Ferroelectric vortices have been realized in various finite-sized nanostructures that allow such constraints to be produced. However, manipulation of topological excitations in otherwise topologically trivial flat ferroelectrics remains a tantalizing challenge. Here we show that a vortex–antivortex pair can be produced by a momentary electric pulse using a tip in a usual Kittel's stripe domain of a BiFeO₃ thin film. Moreover, we demonstrate that the distance between the paired vortex and antivortex can be controlled by dragging the biased tip. The spatial distribution of the local piezoresponse vectors is directly mapped using angle-resolved piezoresponse force microscopy and analyzed by local winding number calculation. Our findings offer a useful concept for the control of topological defects in ferroelectrics.

npj Quantum Materials (2019)4:29; <https://doi.org/10.1038/s41535-019-0167-y>

INTRODUCTION

Topologically non-trivial textures of vector order parameters in real, momentum, and complex-phase spaces form the basis for exotic phenomena.¹ In particular, observing and manipulating the topological objects in ferroic materials has been a fascinating topic that can facilitate energy-efficient, high-density information technologies.² Ferroelectric textures such as vortices, skyrmions, and flux-closure structures^{3–7} have been achieved in various nanostructures due to spatially confined boundary conditions. Topological charge can be also configured by domain flipping in strain graded nanoplatelets,⁸ thereby creating charged domain walls.^{9,10} Recently, research on topological textures in quasi-infinite-sized thin films and bulk crystals has also been pursued, following the discovery of bubble structures and polar vortex arrays in superlattices^{11,12} and self-organized vortices in hexagonal manganites.^{13,14}

The two-dimensional (2D) winding number is invariant under continuous deformation and the total topological charge is protected by the given boundary condition.^{1,8} Modifying the overall topological structure requires a great deal of energy depending on the size of the system, so that no modulation of the topological charge is achieved in an infinite-sized uniform sample. In contrast, the production of a vortex–antivortex pair can be readily realized as a topological excitation because it consumes a small amount of energy in proportion to the logarithmic length of the separation between the vortex and the antivortex.¹⁵ Recently, Li et al. demonstrated the creation of ferroelectric vortex–antivortex pairs using a local electric field.¹⁶ They successfully observed the electric formation of topological networks consisting of two or three vortex–antivortex pairs and temporal evolution of their configurations. Despite the achievement, it remains a tantalizing challenge to create, observe, and

manipulate a *single* vortex–antivortex pair from the aspect of a low-lying elementary excitation. In this context, devising a way to manipulate the positions of the vortex and the antivortex is beneficial for artificially controlling topological defects beyond the discovery of static textures. A tip-induced electric field is a suitable tool for generating vortices in uniform ferroelectrics^{16–19} and deterministically controlling the ferroelectric states.^{16–22}

In this paper, we demonstrate the creation of a *single* vortex–antivortex pair in ferroelectrics and the separation of the pair through tip-induced electric fields in a topologically trivial ferroelectric thin film of BiFeO₃ (BFO) deposited with a bottom electrode SrRuO₃ (SRO) on a (110)_O-oriented DyScO₃ (DSO) substrate (where the subscript “O” represents the orthorhombic index).²³ We clarify the detailed texture of the topologically excited pair with the aid of angle-resolved lateral piezoresponse force microscopy (PFM).^{24–26} Moreover, we analyze the map of experimentally measured piezoresponse vectors by calculating local winding numbers to identify the exact locations of the non-trivial topological charges.

BFO is a representative multiferroic with a strong ferroelectric polarization ($\sim 90 \mu\text{C cm}^{-2}$) at room temperature ($T_C \sim 1100 \text{ K}$).²⁷ BFO in bulk has a rhombohedral unit cell elongated along the same axis of polarization. Its eight possible polarization directions are more appropriate for creating non-collinear configurations of polarizations than the tetragonal ferroelectrics like PbTiO₃. Moreover, BFO has multiple competing phases such as the super-tetragonal structure in highly compressive strains^{28,29} and the orthorhombic structure with $\langle 110 \rangle$ polarizations in tensile strains,^{30,31} and thus we expect that the polymorphic phases can be involved in producing more smoothly revolving vortex textures.

¹Department of Physics, Korea Advanced Institute of Science and Technology (KAIST), Daejeon 34141, Republic of Korea; ²Center for Lattice Defectronics, KAIST, Daejeon 34141, Republic of Korea and ³KAIST Institute for the NanoCentury, KAIST, Daejeon 34141, Republic of Korea
Correspondence: Chan-Ho Yang (chyang@kaist.ac.kr)

Received: 18 January 2019 Accepted: 21 May 2019

Published online: 12 June 2019

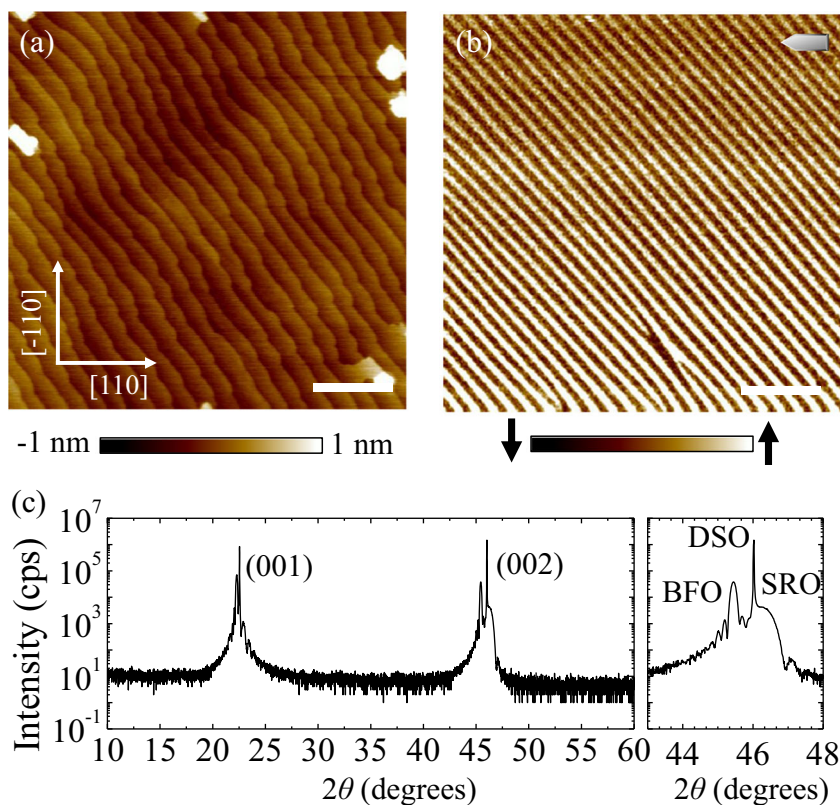


Fig. 1 **a** Surface morphology of the as-grown BFO/SRO/DSO sample. **b** In-plane piezoresponse force microscopic image for the identical sample, taken at a tip orientation displayed by the tip cartoon. Horizontal scale bars represent 1 μm . **c** 2θ - ω scan for the as-grown BFO/SRO/DSO sample. The enlarged view of the (002) peak on the right panel

RESULTS AND DISCUSSION

Sample characterization

The surface morphology in Fig. 1a shows an atomically flat surface with a step-terrace structure indicating the step-flow growth mode during the BFO deposition. The in-plane (IP) PFM image in Fig. 1b indicates that the as-grown BFO thin film has two-variant stripe domains with 71° domain walls. The out-of-plane (OOP) polarization is uniformly downward in the as-grown state (not shown here). This ferroelectric domain structure provides a topologically trivial system without any singular point of ferroelectric polarization.

To characterize crystallinity, X-ray diffraction was carried out by using an X-ray diffractometer (PANalytical X'pert-PRO MRD) with $\text{Cu } K\alpha_1$ radiation ($\lambda \sim 1.5406 \text{ \AA}$). Figure 1c displays a conventional 2θ - ω scan where no noticeable impurity peaks are detected except for the film and substrate peaks in the wide range of scan angles. The c axis lattice parameter of BFO was measured to be 3.98 \AA and those of SRO and DSO were 3.92 and 3.94 \AA , respectively. A zoomed-in graph around pseudocubic (002) peaks on the right-hand side of the figure shows clear Kiessig fringes and the oscillation period of the fringes around the film peak enables us to estimate film thickness to be 53 nm .

Experimental design to create and separate a topological pair

Electric fields induced by a tip create stray fields around the tip along concentric inward directions when a negative bias is applied to the tip.^{16–22} Figure 2a shows a schematic of local polarization switching. Applying a negative bias to a point in a uniformly polarized medium induces a ferroelectric vortex underneath the tip. To decrease the polarization gradient energy, polarizations are rotated across the boundaries between the switching region and

the as-grown region continuously. If we perform local poling using a negative voltage in a uniformly leftward polarized domain, the upper (lower) boundary has counter-clockwise (clockwise) chirality of the domain wall because the polarizations on the boundary rotate along the acute angle. The domain wall with cyan color has clockwise chirality, and another domain wall with magenta color has counter-clockwise chirality. The two chiral domain walls encounter each other at the left side of the vortex point, and this singular point forms an antivortex. The magnified schematic diagrams near the antivortex show polarization rotations across the chiral domain walls. Therefore, a single vortex and a single antivortex are paired within the poled region.

When the orientations of piezoresponse vectors vary continuously, the 2D winding number along a closed loop L is defined as

$$n = \frac{1}{2\pi} \oint_L \nabla\theta \cdot d\mathbf{r} \quad (1)$$

where θ denotes the IP orientation angle of the piezoresponse vector.^{1,8} Figure 2b shows the expected local winding number calculations over the polarization switching region. By performing a local winding number calculation on each square loop, we will be able to identify the existence of a single vortex that gives a winding number equal to $+1$ for the central loop. An antivortex that gives the winding number of -1 is found on the left side of the vortex point. Near the antivortex, the polarizations on its left or right domains orient in directions outward from the antivortex, but the polarizations at the vertically aligned domain walls point to the inward directions, thereby creating a two-in-two-out configuration of electric polarizations.

However, because the as-grown domain structure of the BFO/SRO/DSO film is unlike the uniform domain, the description needs

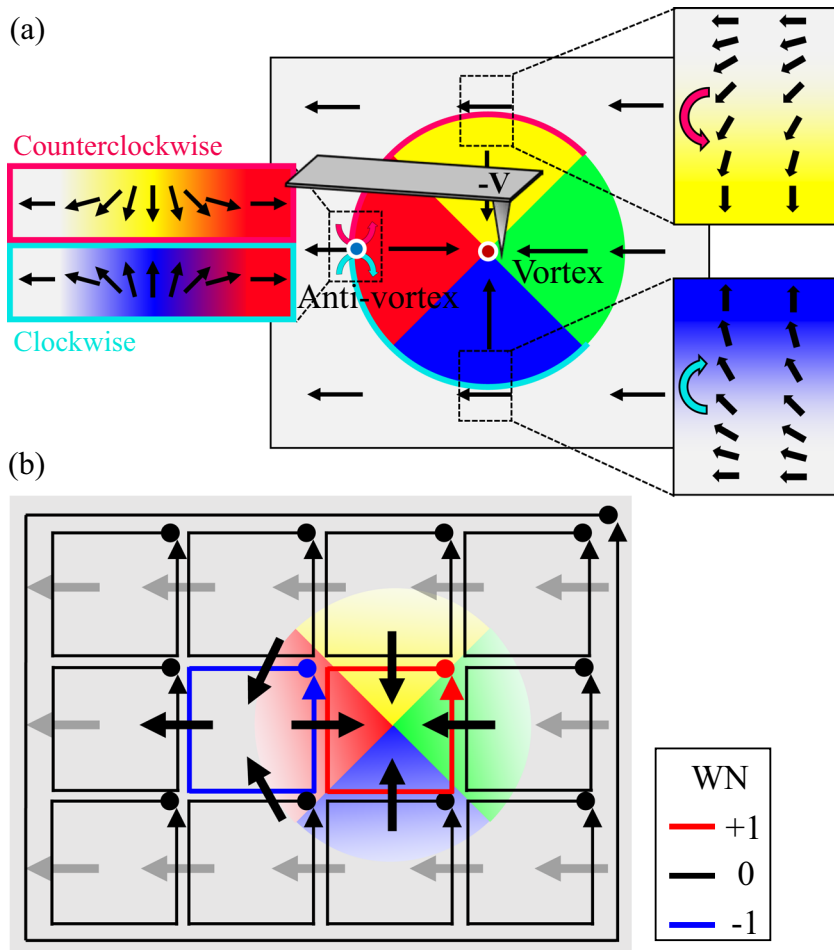


Fig. 2 Schematic illustration of vortex–antivortex pair creation by the application of a localized electric pulse generated by a negatively biased tip. **a** As the ferroelectric polarization gradually rotates along an acute angle across the domain wall, the clockwise (cyan) or counterclockwise (magenta) chirality of the domain wall is clamped along the boundary of the poling region. An antivortex must exist at a point where two different chiral domain walls are encountered. **b** Electric polarizations are distributed continuously everywhere except singular points. The square-closed loops were laid to calculate the local winding number around each loop. The red, gray, and blue loops represent the winding numbers $+1$, 0 , and -1 , respectively. Note that the large loop along the outer boundary of the displayed region also has a winding number of zero due to nulling of the two singularities

to be modified. Although the lattice mismatch between the BFO film and DSO $(110)_O$ substrate is small ($\sim 0.25\%$), the substrate applies anisotropic IP strains to the BFO film, so that the BFO film forms two-variant stripe domain patterns with 71° domain walls,²³ which are topologically trivial (Fig. 1b). Creation of a vortex in a finite poling area guarantees the existence of an antivortex nearby. The schematic in Fig. 3a shows the expected texture, which is poled by an electric pulse using a negatively biased tip. Similarly, a vortex will appear at the center as a result of inwardly converging IP polarizations. Since the as-grown domains have $\langle 110 \rangle$ directional IP polarizations in this case, the position of the antivortex is also changed to the upper left corner by 45° rotation.

To manipulate the vortex and antivortex point separately, we need to move the vortex point by dragging the biased tip, as shown in Fig. 3b. As the tip is dragged, the inward trailing fields of the tip make the yellow and red domains expand. When the tip is moving to the right, the tip-induced fields on the right-hand side of the tip are erased by the following fields on the left-hand side of the tip. Exceptionally, at the final position of the tip, the tip-induced stray fields given to the right-hand side of the tip survive. As a result, the vortex follows the motion of the tip and is located at the final position of the tip. As a result, we can control the distance between the vortex and the antivortex arbitrarily.

High-resolution angle-resolved lateral PFM

Direct visualization of topological ferroelectric textures is essential for implementing the designed procedures experimentally and exploring the detailed topological features. We will employ the high-resolution angle-resolved lateral PFM.^{24,25} Since the lateral PFM technique relies on the torsional vibration mode of the cantilever, only the component projected to an IP axis perpendicular to the cantilever is distinguished. Based on several independent scans with different cantilever orientations, IP piezoelectric response at each point can be determined by integrating all the scan data and performing the trigonometric curve fitting for the PFM signals with respect to the tip orientation angle (Fig. 4). During PFM measurements, various extrinsic tip drift issues, e.g., arising from the hysteresis of a piezoelectric actuator, can distort the measured images. It is needed to align PFM images taken in different tip orientation angles pixel by pixel. For this, we have developed an image registration algorithm.²⁵

The first step of the alignment is to find a linear transformation matrix between paired reference points handpicked in two given images (e.g., from peculiar points in topography or domain walls). We adopted the affine transformation, which allows translation, rotation, scale, and shear deformation, to transform from a point (x_1, y_1) in image 1 to a point (x_2, y_2) in image 2. We can express the

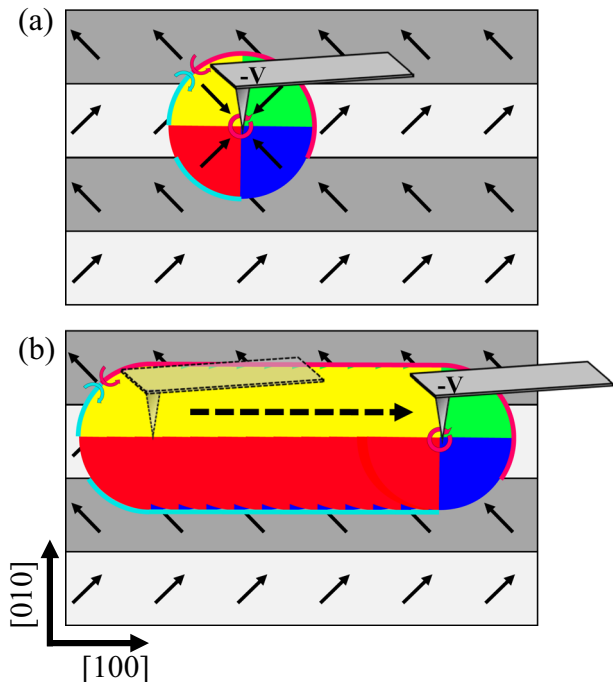


Fig. 3 **a** Creation of a vortex–antivortex pair in striped ferroelectric domains. The cyan and magenta colors on the domain walls represent clockwise and counterclockwise chirality, respectively. The antivortex is located at the point where two different chiral domain walls collide. In this domain configuration, the antivortex is created in the upper left domain wall. **b** The vortex–antivortex pair separation is performed by dragging the negative probe from left to right. The vortex point follows the tip motion while the antivortex maintains its original position, thereby the distance can be controlled by the tip dragging length

generic transformation as follow:

$$\begin{bmatrix} x_2 \\ y_2 \end{bmatrix} = \begin{bmatrix} M_{11} & M_{12} \\ M_{21} & M_{22} \end{bmatrix} \begin{bmatrix} x_1 \\ y_1 \end{bmatrix} + \begin{bmatrix} M_{13} \\ M_{23} \end{bmatrix}. \quad (2)$$

To determine the values of coefficients M_{ij} , six independent equations are needed. In other words, three independent reference coordinate sets are at least required to avoid the underdetermined problem. Sufficient numbers of coordinate sets are required for reliably determining the coefficients. Provided we choose N reference points, we find the least square solution for the six matrix elements M_{ij} via minimizing the residual sum of squares:

$$\sum_{a=1}^N \left[(x_2^a - (M_{11}x_1^a + M_{12}y_1^a + M_{13}))^2 + (y_2^a - (M_{21}x_1^a + M_{22}y_1^a + M_{23}))^2 \right], \quad (3)$$

where a stands for the index of reference points. The coefficients can be explicitly expressed as

$$\begin{bmatrix} M_{11} \\ M_{12} \\ M_{13} \\ M_{21} \\ M_{22} \\ M_{23} \end{bmatrix} = (A^T A)^{-1} A^T B,$$

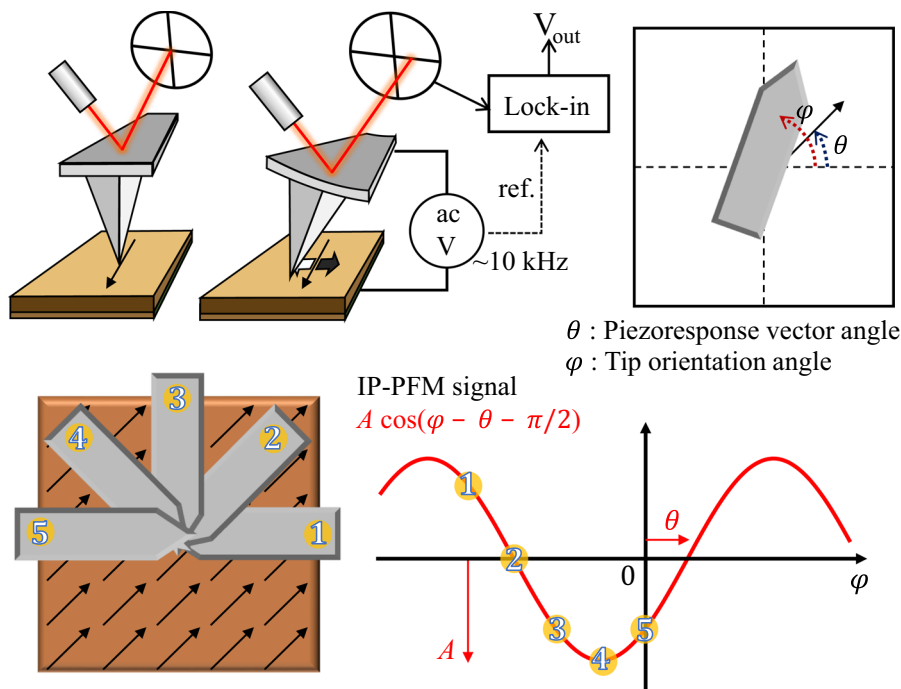


Fig. 4 Schematic of angle-resolved lateral piezoresponse force microscopy (PFM). We collected the in-plane (IP) PFM real part signal experimentally as a function of tip orientation angle φ and then we determined the amplitude and the phase delay, by trigonometric curve fitting, i.e. A and θ in $A \sin(\varphi - \theta)$. Piezoresponse vector field can be constructed by finding IP vector components ($A \cos \theta$, $A \sin \theta$) as a function of position. In the following experiments, the tip orientation angle will be redefined as $\varphi + 180^\circ$

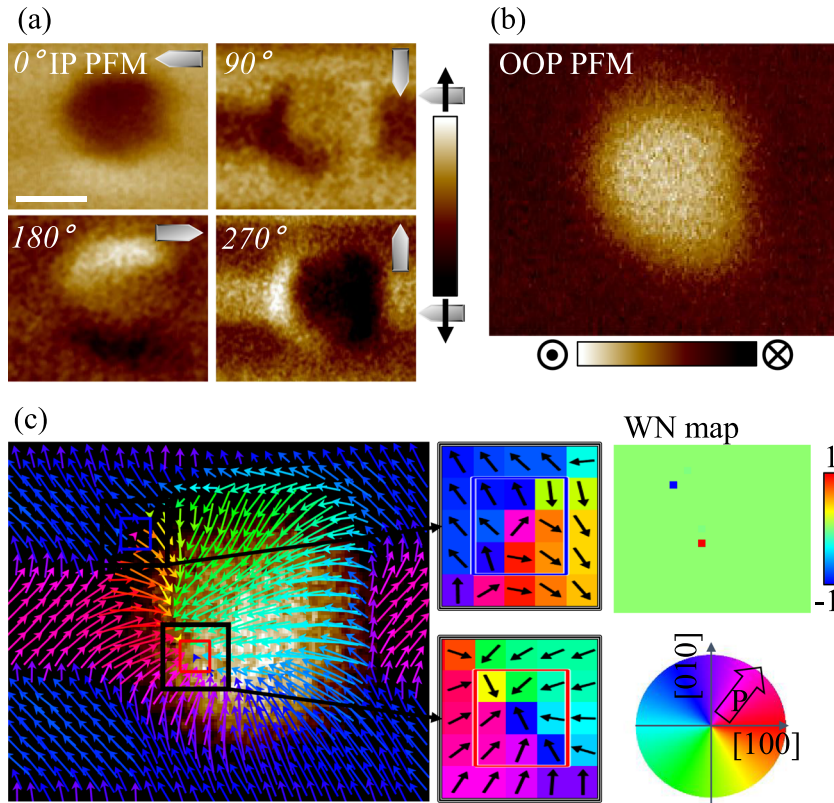


Fig. 5 **a** In-plane piezoresponse force microscopic (IP PFM) images measured in the various cantilever directions indicated by tip cartoons in the upper right corner of each. The scale bar represents 100 nm. **b** Out-of-plane (OOP) PFM image from the identical region. **c** Map of the IP piezoresponse vectors. The background contrast means the OOP PFM signal. The arrow color represents the direction of the IP piezoresponse vector, as indicated in the color wheel. A vortex and an antivortex are observed at the interior and at the border of the poled area, respectively. Each pixel with an arrow has an area of $9.77 \times 9.77 \text{ nm}^2$. The locations of the singular points are clearly identified by local winding number calculation (WN map)

where

$$A = \begin{bmatrix} x_1^1 & y_1^1 & 1 & 0 & 0 & 0 \\ x_1^2 & y_1^2 & 1 & 0 & 0 & 0 \\ \vdots & \vdots & \vdots & \vdots & \vdots & \vdots \\ x_1^N & y_1^N & 1 & 0 & 0 & 0 \\ 0 & 0 & 0 & x_1^1 & y_1^1 & 1 \\ 0 & 0 & 0 & x_1^2 & y_1^2 & 1 \\ \vdots & \vdots & \vdots & \vdots & \vdots & \vdots \\ 0 & 0 & 0 & x_1^N & y_1^N & 1 \end{bmatrix}, B = \begin{bmatrix} x_2^1 \\ x_2^2 \\ \vdots \\ x_2^N \\ y_2^1 \\ y_2^2 \\ \vdots \\ y_2^N \end{bmatrix}. \quad (4)$$

To reduce human errors in the selection of the reference points, further refinements in the transformation coefficients can be made through the Monte Carlo algorithm by updating the coefficients to maximize the overlap function of step terrace edges and/or OOP domain walls that can be extracted from each map by using the Canny edge detection algorithm.²⁵

Creation of a single vortex–antivortex pair

To implement the idea for creation of a single topological pair, we applied -10 V with a pulse width of 0.5 s to the surface of the BFO using a tip (Fig. 5). A circularly shaped poled area with a diameter

of $\sim 100 \text{ nm}$ was formed by reversal of the OOP polarization from the downward one in the as-grown state to an upward one. IP PFM images were obtained at tip orientation angles of 0° , 90° , 180° , and 270° . By using the image alignment algorithm, we were able to construct a map of the IP piezoresponse vectors, as shown in Fig. 5c.

A vortex was made at the central region of the poling and an antivortex was emergent on the upper left corner, which was consistent with our expectation. Because we used a negatively biased tip, stray fields around the tip were inward directed, and thus the IP piezoresponse vectors were aligned to the local electric fields, thereby creating the vortex at the merging point. Although this rhombohedral BFO phase had polarizations along the $\langle 111 \rangle$ axes, large deviations of the polarizations from the polar axes were observed in the whirling IP polarization structure. BFO has been known to have a competing phase called the orthorhombic structure, in which polarizations are on the $\langle 110 \rangle$ axes.^{30,31} Considering that the OOP polarization is upward, the IP polarization of the orthorhombic phase is parallel to $\langle 100 \rangle$. Indeed, the right-hand side region of the vortex has a quite large area where the polarizations are stabilized almost along $[-100]$ (pale blue). The emergence of the metastable phase is helpful for the gradual variation of the IP polarizations.

To clearly identify the locations of singular points, we conducted local winding number calculations around 3×3 square loops tiled on the vector map sharing the edges with neighboring loops. Most of the regions had a winding number of zero except for the two singular points ($+1$ for the vortex and -1 for the antivortex). We note the IP piezoresponse vectors near the

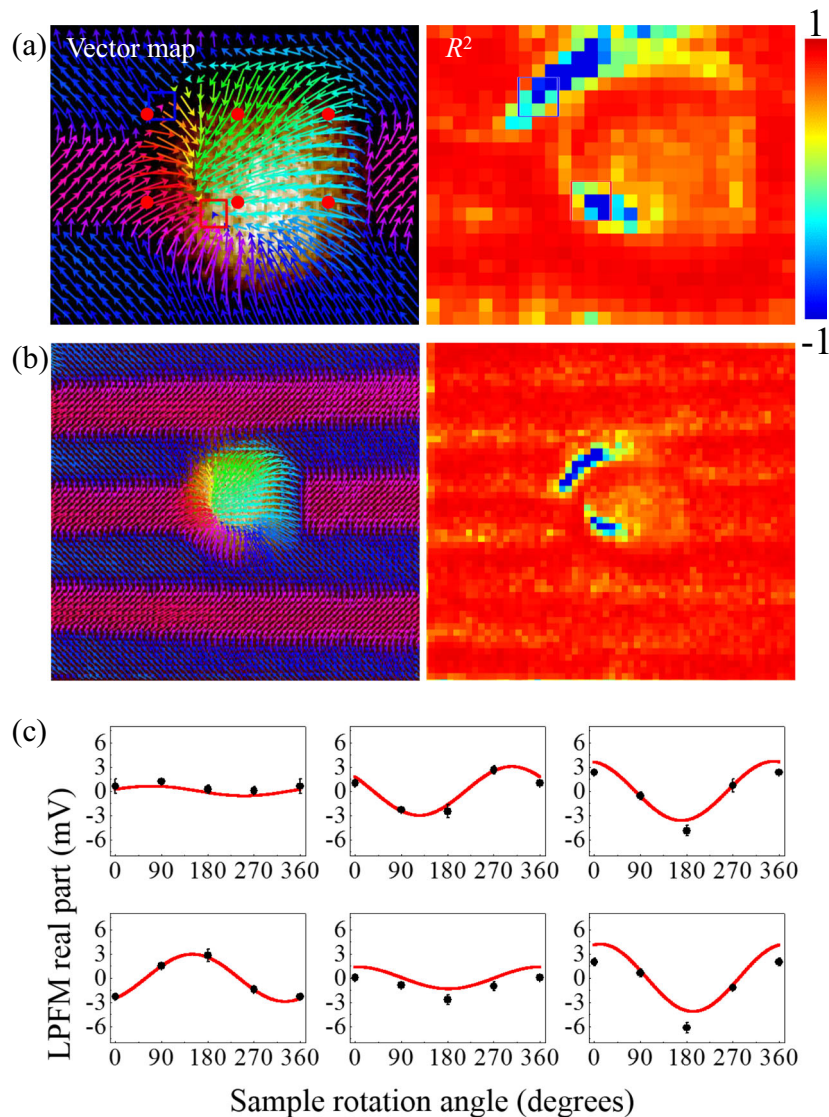


Fig. 6 **a** In-plane (IP) piezoresponse vector map for a vortex–antivortex pair produced by applying an electrical pulse. Reliability for the sinusoidal fitting is examined by the plot of R^2 on the right. Regions near the two singular points exhibit large deviations of R^2 from the ideal value of 1. This is attributed to the small magnitude of IP piezoresponse force microscopic signals stemming from ferroelectric instability and associated electrical frustration near the vortices. **b** A zoomed out view of the topological defects pair. **c** The trigonometric curve fitting for six representative points that are denoted as red spots in **a**

singular points become relatively small in magnitude to minimize the Ginzburg energy associated with the polarization gradient. So the detailed structures at the singular points seem to be vulnerable to intrinsic/extrinsic fluctuations of the polarization distribution.

To assess the reliability of the trigonometric fittings for constructing the vector map, Fig. 6a, b presents a map of R-squared (R^2) over the region and a map over a larger area. We also plot the sinusoidal fitting curves with the raw data of IP piezoresponses acquired as a function of tip orientation at six representative points in the switched region (Fig. 6c). It is seen that the two singular points have a large deviation of R^2 from +1 that means the trigonometric fittings therein are far from the ideal situation. It is because the singular points have small PFM signals less than our instrumental sensitivity. By a careful look at the raw data in the Fig. 6c, we can recognize that the lateral PFM data have a small offset that can arise from tip asymmetry. All instruments have their own limitation of sensitivity. When the

signal is smaller than or comparable to the limitation, we should be cautious in interpreting the data.

Even if we have uncertainty in the core regions of topological points, we can still safely argue that the areas have topological singularities. The topological defects are not local defects but global textures. The topological winding number calculated along a given closed loop is equal to the net number of topological charges (+1 for a vortex and -1 for an antivortex) enclosed by the closed loop. So, any arbitrary closed loop results in the same winding number as long as the loop contains the same singular points. Thus the topological feature of the system is very robust against perturbations. Even though we intentionally flip piezoresponse vectors at sparse random sites, the local winding number map does not change. Ironically, such R^2 map can be used as an indicator of topological singular points.

The striped domain structure in the as-grown state is a topologically trivial space and thus winding number calculation around any closed loop on the surface results in zero. This result is

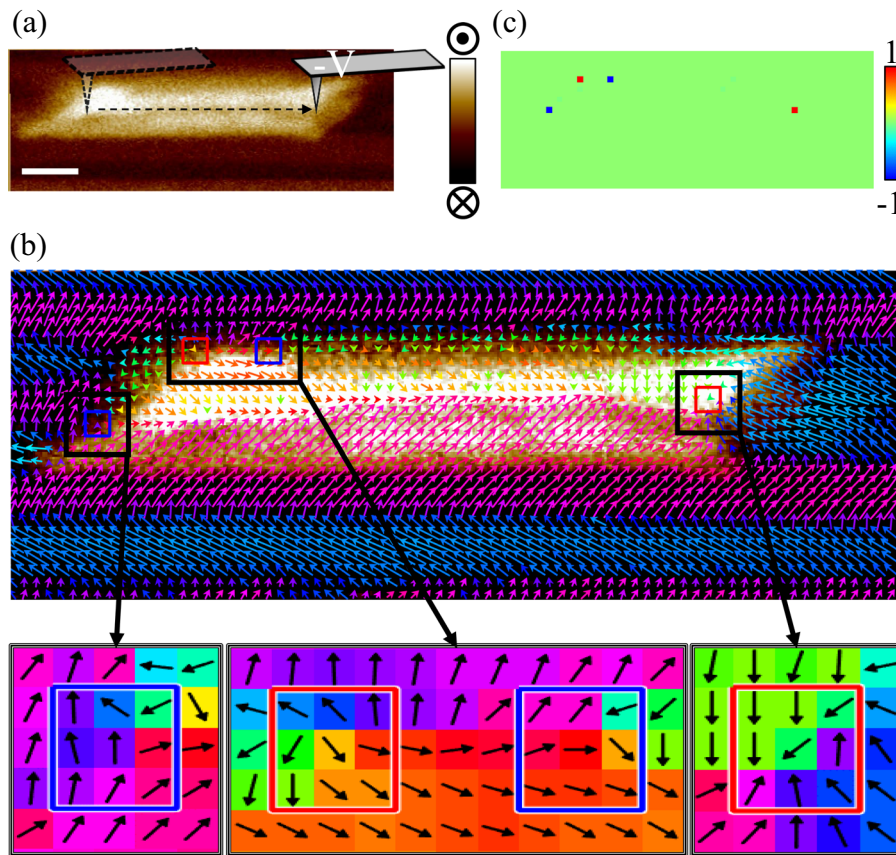


Fig. 7 **a** Out-of-plane (OOP) piezoresponse force microscopic (PFM) image after electrical tip dragging. The electrical writing was made by dragging the negative biased tip from left to right. The scale bar indicates 200 nm. **b** IP piezoresponse vector map constructed by analyzing four IP PFM images measured with tip orientations of 0° , 45° , 90° , 135° in an integrated manner. The map is displayed on the OOP PFM contrast. The antivortex is pinned at the left boundary of the poled area, but the vortex moves to the right-hand side following the tip motion. An additional vortex–antivortex pair in the left central region was created unintentionally. Each pixel with an arrow has an area of $19.53 \times 19.53 \text{ nm}^2$. **c** Local winding number map

the same for a closed loop that is sufficiently large enough to include the poling area. The winding number for a large loop is equal to the total sum of local winding numbers for all small sub-areas contained in the large loop (Fig. 2b). Accordingly, the existence of the vortex in the trivial space guarantees the existence of an antivortex somewhere nearby. By using the angle-resolved PFM, we directly identified the location of the antivortex.

The vortex–antivortex pair in the 2D XY spin model undergoes an attractive interaction¹⁵ and eventually pair annihilation happens, erasing the poling effect. Interestingly, this topological texture appears to be quasi-stable. Even when we performed several PFM scans, the texture endured the perturbations and remained nearly the original configuration. The interaction between the topological charges in this rhombohedral ferroelectric is more complex than the simple 2D XY model and most likely is involved in the short-range repulsive interaction associated with the change in the OOP polarization. This pair is reminiscent of the bound state of the bimeron as discussed theoretically in frustrated magnets.³²

Separation of a single vortex–antivortex pair

The negatively biased tip was dragged to the right by $1 \mu\text{m}$ to separate the vortex–antivortex pair, using the strategy previously described. This electric line scan induced an upward poling region

with a $1 \mu\text{m} \times 200 \text{ nm}$ area as shown in Fig. 7a. We constructed the IP PFM vector map by integrating IP PFM images measured at four different tip orientation angles (Fig. 7b). The resultant domain texture contained various domain walls and metastable phases. For example, we recognized a 71° domain wall along the bottom horizontal line due to the fact that the OOP polarization is reversed, but the IP polarization does not change. We also observe a charged domain wall along the central line of the scan, where 109° domain switching of the IP polarization occurs, and the IP polarizations merge to the domain wall. We also observed that the upper right region had an orthorhombic polarization along $[0-10]$ as indicated by the green color.

This vector mapping using the angle-resolved lateral PFM provides a powerful tool for further scrutinizing the topological features quantitatively. We calculated local winding numbers for the edge-shared square loops that are arranged on the vector map to identify the locations of topological points. We detected the existence of two vortices and two antivortices as described in Fig. 7c. The first electric pulse at the initial moment of the scan generates the antivortex on the left edge as well as the central vortex. Using the line scan, we moved the central vortex to the right edge. The singular points on the two ends are attributed to the separation of the vortex–antivortex pair. Although we noticed an additional pair was unintentionally produced on the left central region, we were able to demonstrate the original idea of separating the topological defects by the tip dragging method.

Small ferroelectric domains typically have a short retention time. This is because the domain wall energy at the boundary of a small polling area makes the free energy of the system unstable despite the energy gain of the depolarization energy due to the relatively large boundary-to-area ratio. This has been an obstacle to developing high-density ferroelectric data storage devices comprising of small bits. From the perspective of the topology, we expect to be able to describe the domain shrinkage and loss of a small polling domain by vortex–antivortex pair annihilation. Understanding the mutual attraction between topological defects that are arbitrarily separated by tip dragging is an interesting future topic potentially related to enhancement of the retention time.

In summary, we created a vortex–antivortex pair in a rhombohedral ferroelectric BFO using a tip-induced electric pulse and controlled the distance between the vortex and the antivortex via a single line scan with a biased tip. By directly observing the piezoresponse vector distribution by angle-resolved lateral PFM, we were able to identify the exact locations of the topological defects and perform the topological analysis by local winding number calculation. Our finding provides a new avenue into the creation and control of vortex and antivortex points in topologically trivial flat ferroelectrics.

METHODS

Sample preparation

An epitaxial ~50-nm-thick BFO thin film was deposited on a (110)_O-oriented orthorhombic DSO substrate with an in-situ grown 10-nm-thick SRO bottom electrode using pulsed laser deposition equipped with a KrF excimer laser (with a wavelength of 248 nm). The growth was made at 705 °C in an oxygen environment of 100 mTorr. The laser fluence was 1.17 J cm⁻² with a repetition rate of 10 Hz. After the growth was completed, the sample was cooled to room temperature at a rate of 10 °C min⁻¹ in an oxygen environment of 500 Torr to minimize the creation of oxygen vacancies.

Piezoresponse force microscopy

The surface morphology and ferroelectric domains of BFO were characterized using a scanning probe microscope (Bruker MultiMode V equipped with a Nanoscope controller V) with Pt-coated Si tips (HQ:NSC35/Pt, MikroMasch). The PFM measurements were performed at a scanning rate of ~2.1 μm s⁻¹ applying an ac driving voltage 3 V at a frequency of 10 kHz in ambient conditions. Since IP PFM only measures the component perpendicular to the cantilever axis, which is associated with the torsional vibration of the cantilever, we gathered the real part images of IP PFM signals measured at different probe orientations to construct a full vector map of the IP piezoresponse vector.

DATA AVAILABILITY

The data that support the findings of this study will be available from the corresponding author upon reasonable request.

ACKNOWLEDGEMENTS

This work was supported by National Research Foundation (NRF) Grants funded by the Korean Government via the Creative Research Initiative Center for Lattice Defectronics (2017R1A3B1023686) and the Center for Quantum Coherence in Condensed Matter (2016R1A5A1008184).

AUTHOR CONTRIBUTIONS

C.-H.Y. initiated and supervised the project. J.K. and M.Y. measured the PFM images. J.K., M.Y., K.-E.K., and K.C. analyzed the data using the angle-resolved PFM technique and the winding number calculation. J.K. and C.-H.Y. wrote the manuscript.

ADDITIONAL INFORMATION

Competing interests: The authors declare no competing interests.

Publisher's note: Springer Nature remains neutral with regard to jurisdictional claims in published maps and institutional affiliations.

REFERENCES

1. Mermin, N. D. The topological theory of defects in ordered media. *Rev. Mod. Phys.* **51**, 591–648 (1979).
2. Seidel, J. (ed) *Topological structures in ferroic materials* (Springer International Publishing, Cham, 2016).
3. Gregg, J. M. Exotic domain states in ferroelectrics: searching for vortices and skyrmions. *Ferroelectrics* **433**, 74–87 (2012).
4. Schilling, A. et al. Domains in ferroelectric nanodots. *Nano Lett.* **9**, 3359–3364 (2009).
5. Naumov, I. I., Bellaiche, L. & Fu, H. Unusual phase transitions in ferroelectric nanodisks and nanorods. *Nature* **432**, 737–740 (2004).
6. Li, Z. et al. High-density array of ferroelectric nanodots with robust and reversibly switchable topological domain states. *Sci. Adv.* **3**, 1700919 (2017).
7. Nahas, Y. et al. Discovery of stable skyrmionic state in ferroelectric nano-composites. *Nat. Commun.* **6**, 8542 (2015).
8. Kim, K.-E. et al. Configurable topological textures in strain graded ferroelectric nanoplates. *Nat. Commun.* **9**, 403 (2018).
9. Ma, J. et al. Controllable conductive readout in self-assembled, topological confined ferroelectric domain walls. *Nat. Nanotechnol.* **13**, 947–952 (2018).
10. Kim, K.-E. et al. Ferroelastically protected polarization switching pathways to control electrical conductivity in strain-graded ferroelectric nanoplates. *Phys. Rev. Mater.* **2**, 084412 (2018).
11. Zhang, Q. et al. Nanoscale bubble domains and topological transitions in ultrathin ferroelectric films. *Adv. Mater.* **29**, 1702375 (2017).
12. Yadav, A. K. et al. Observation of polar vortices in oxide superlattices. *Nature* **530**, 198–201 (2016).
13. Chae, S. C. et al. Self-organization, condensation, and annihilation of topological vortices and antivortices in a multiferroic. *Proc. Natl Acad. Sci. USA* **107**, 21366–21370 (2010).
14. Huang, F.-T. & Cheong, S.-W. Aperiodic topological order in the domain configurations of functional materials. *Nat. Rev. Mater.* **2**, 17004 (2017).
15. Kosterlitz, J. M. & Thouless, D. J. Ordering, metastability and phase transitions in two dimensional systems. *J. Phys. C Solid State Phys.* **6**, 1181 (1973).
16. Li, Y. et al. Rewritable ferroelectric vortex pairs in BiFeO₃. *npj Quantum Mater.* **2**, 43 (2017).
17. Balke, N. et al. Deterministic control of ferroelastic switching in multiferroic materials. *Nat. Nanotechnol.* **4**, 868–875 (2009).
18. Vasudevan, R. K. et al. Exploring topological defects in epitaxial BiFeO₃ thin films. *ACS Nano* **5**, 879–887 (2011).
19. Balke, N. et al. Enhanced electric conductivity at ferroelectric vortex cores in BiFeO₃. *Nat. Phys.* **8**, 81–88 (2012).
20. Kim, K.-E. et al. Electric control of straight stripe conductive mixed-phase nanostructures in La-doped BiFeO₃. *NPG Asia Mater.* **6**, e81 (2014).
21. Lee, J. H., Chu, K., Kim, K.-E., Seidel, J. & Yang, C.-H. Out-of-plane three-stable-state ferroelectric switching: finding the missing middle states. *Phys. Rev. B* **93**, 115142 (2016).
22. Park, S. M. et al. Selective control of multiple ferroelectric switching pathways using trailing flexoelectric field. *Nat. Nanotechnol.* **13**, 366–370 (2018).
23. Chu, Y.-H. et al. Nanoscale domain control in multiferroic BiFeO₃ thin films. *Adv. Mater.* **18**, 2307–2311 (2006).
24. Chu, K. et al. Enhancement of the anisotropic photocurrent in ferroelectric oxides by strain gradients. *Nat. Nanotechnol.* **10**, 972–979 (2015).
25. Chu, K. & Yang, C.-H. High-resolution angle-resolved lateral piezoresponse force microscopy: visualization of in-plane piezoresponse vectors. *Rev. Sci. Instrum.* **89**, 123704 (2018).
26. Park, M. et al. Three-dimensional ferroelectric domain imaging of epitaxial BiFeO₃ thin films using angle-resolved piezoresponse force microscopy. *Appl. Phys. Lett.* **97**, 112907 (2010).
27. Fischer, P., Polomska, M., Sosnowska, I. & Szymanski, M. Temperature dependence of the crystal and magnetic structures of BiFeO₃. *J. Phys. C Solid State Phys.* **13**, 1931 (1980).
28. Ko, K.-T. et al. Concurrent transition of ferroelectric and magnetic ordering near room temperature. *Nat. Commun.* **2**, 567 (2011).
29. Woo, C.-S. et al. Suppression of mixed-phase areas in highly elongated BiFeO₃ thin films on NdAlO₃ substrates. *Phys. Rev. B* **86**, 054417 (2012).

30. Yang, J. C. et al. Orthorhombic BiFeO₃. *Phys. Rev. Lett.* **109**, 247606 (2012).
31. Lee, J. H. et al. Phase separation and electrical switching between two isosymmetric multiferroic phases in tensile strained BiFeO₃ thin films. *Phys. Rev. B* **89**, 140101(R) (2014).
32. Kharkov, Y. A., Sushkov, O. P. & Mostovoy, M. Bound states of skyrmions and merons near the Lifshitz point. *Phys. Rev. Lett.* **119**, 207201 (2017).



Open Access This article is licensed under a Creative Commons Attribution 4.0 International License, which permits use, sharing, adaptation, distribution and reproduction in any medium or format, as long as you give

appropriate credit to the original author(s) and the source, provide a link to the Creative Commons license, and indicate if changes were made. The images or other third party material in this article are included in the article's Creative Commons license, unless indicated otherwise in a credit line to the material. If material is not included in the article's Creative Commons license and your intended use is not permitted by statutory regulation or exceeds the permitted use, you will need to obtain permission directly from the copyright holder. To view a copy of this license, visit <http://creativecommons.org/licenses/by/4.0/>.

© The Author(s) 2019